Supporting Information for

Sublimation-based wafer-scale monolayer WS_2 formation via self-limited thinning of few-layer WS_2

Mingxi Chen[1], Jianwei Chai[1], Jing Wu[1], Haofei Zheng[1,2], Wen-Ya Wu[1], James Lourembam[1], Ming Lin[1], Jun-Young Kim[1], Jaewon Kim[1], Kah-Wee Ang[1,2], Man-Fai Ng[3], Henry Medina[,1], Shi Wun Tong[*,1], and Dongzhi Chi[*,1]*

1 Institute of Materials Research and Engineering (IMRE), Agency for Science, Technology and Research (A*STAR), 2 Fusionopolis Way, Innovis #08-03, Singapore 138634, Republic of Singapore

2 Department of Electrical and Computer Engineering, National University of Singapore, 4 Engineering Drive 3, Singapore 117583, Republic of Singapore

3 Institute of High Performance Computing (IHPC), Agency for Science, Technology and Research (A*STAR), 1 Fusionopolis Way, #16-16 Connexis, Singapore 138632, Republic of Singapore

*The correspondence should be addressed to D. Chi (dz-chi@imre.a-star.edu.sg), S. W. Tong (tongsw@imre.a-star.edu.sg) and H. Medina (Henry.MedinaSilva@imec.be).

This file includes:

Figure S1 to S11

Table S1

1. **Comparison of Raman and PL spectra between PSS-WS_2 film and single crystal monolayer and bilayer WS_2.**

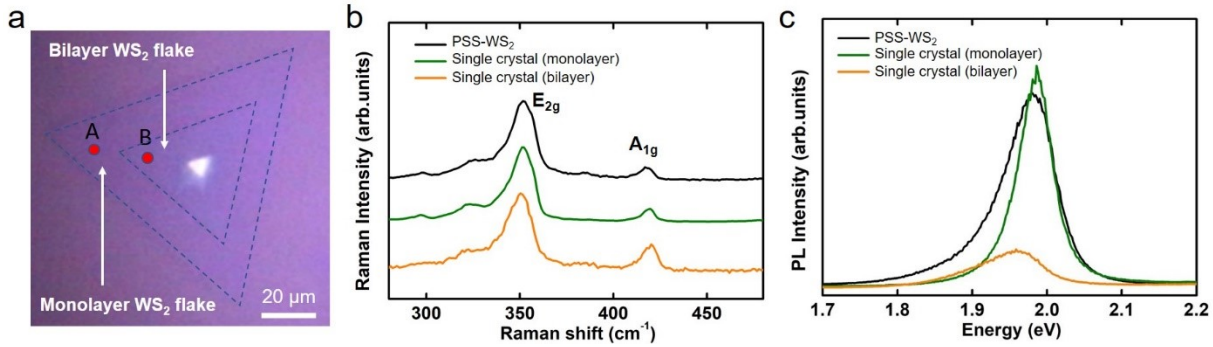

Figure S1. (a) Optical micrograph image of triangular shape WS_2 flakes containing a second layer smaller triangular shape WS_2 domain. Comparisons of (b) Raman and (c) PL spectra of the PSS-WS_2 film against those from single crystal monolayer and bilayer WS_2, respectively.

2. **Raman and PL spectra collected on different positions of the PVD-WS_2 film before and after the thinning process.**

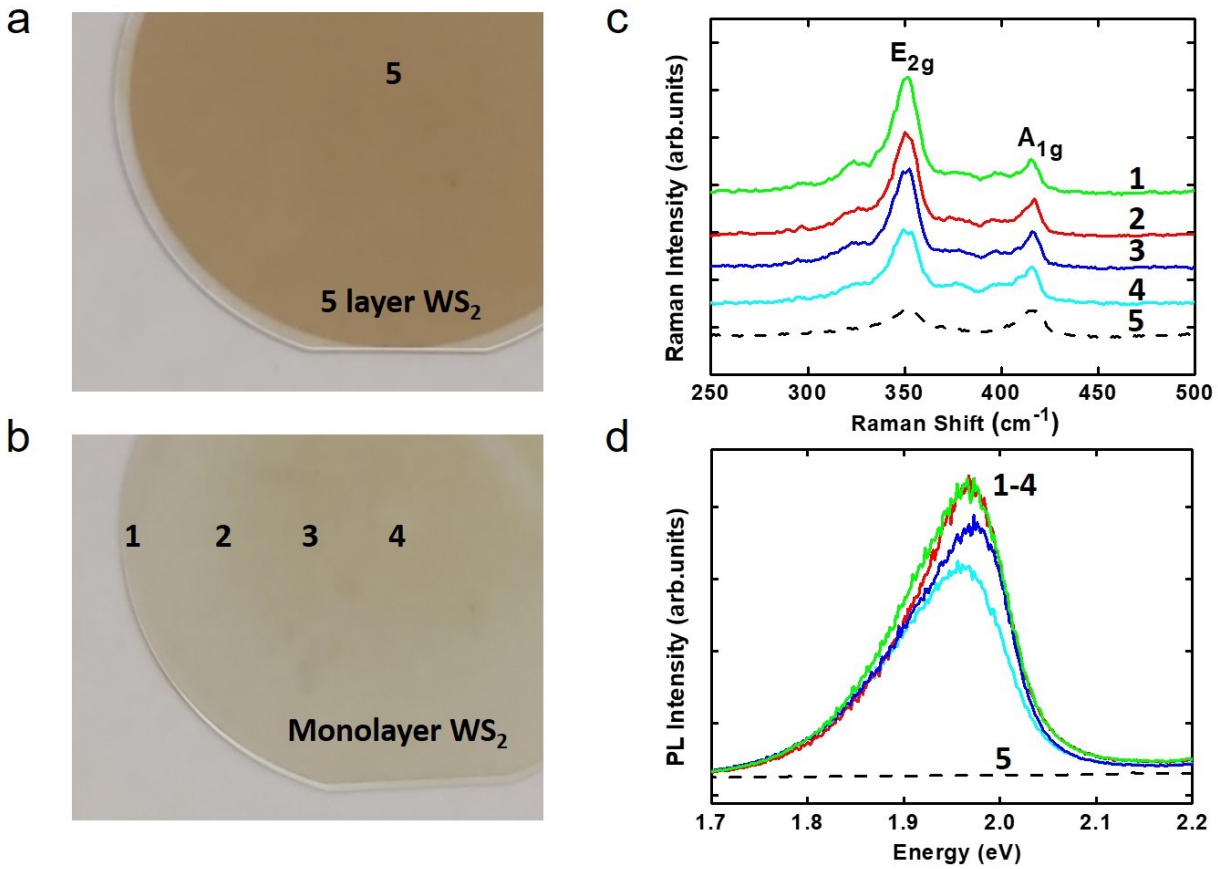

Figure S2. Photographs of the few-layer sputter deposited PVD-WS_2 on the 2-inch sapphire substrate (a) before and (b) after the self-limited thinning process at temperature of 1000 °C. Comparisons of the corresponding (c) Raman and (d) photoluminescence spectra collected on different positions of the PVD-WS_2 film before (spot 5) and after (spots 1-4) the thinning process. The intensity ratio of A_{1g}/E_{2g} measured on multiple locations of PVD-WS_2 is decreased from 1 to ~ 0.28 after the PSS process confirms the few-layer WS_2 has been thinned down into monolayer thick. The formation of monolayer WS_2 is further evidenced by the observation of a strong PL peak at ~1.98 eV (spots 1-4).

3. **Raman and PL spectra collected on different positions of the PVD-MoS_2 film before and after the thinning process.**

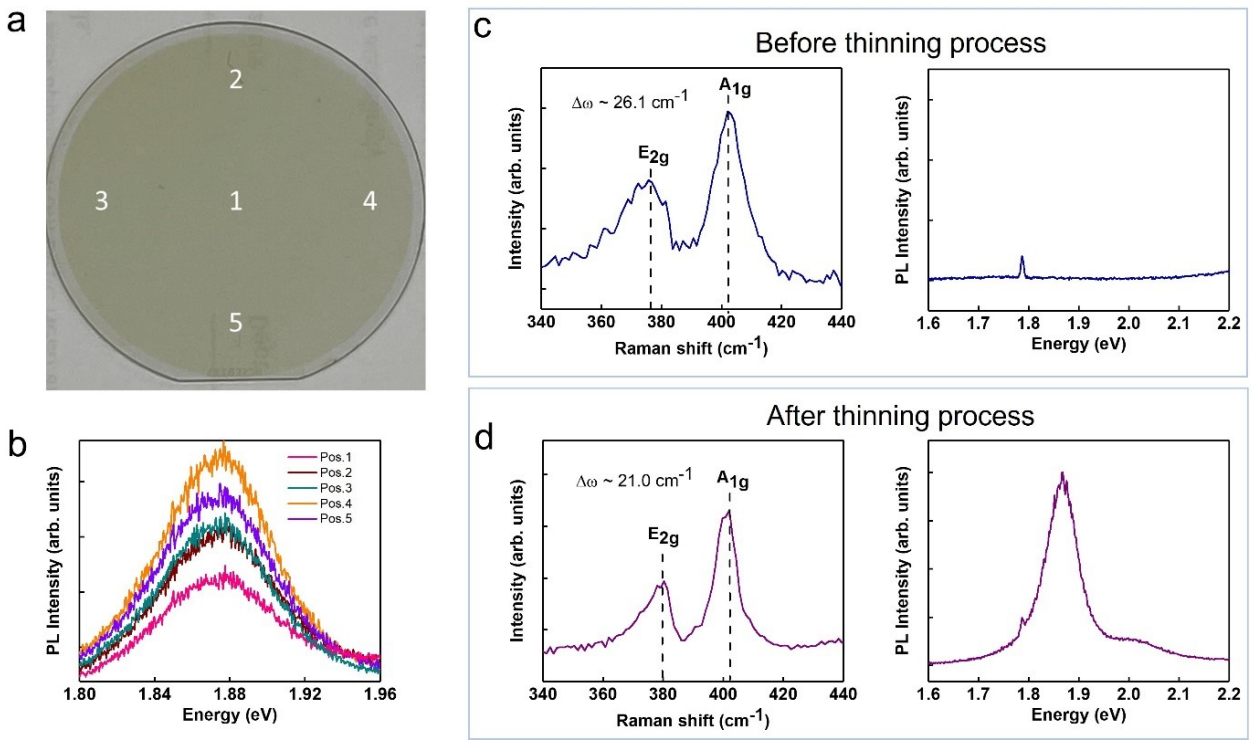

Figure S3. (a) Photograph and (b) the photoluminescence spectra of the monolayer PVD-MoS_2 on the 2-inch sapphire substrate after the self-limited thinning process at temperature of 950 °C. Comparisons of the Raman and photoluminescence spectra detected from PVD-MoS_2 film (c) before and (d) after the thinning process. Few-layer MoS_2 films are prepared by PVD sputtering process which have been reported in our previous works.[1,2] After the thinning process, there is a significant drop in frequency difference between E_{2g} and A_{1g} peaks ($\Delta\omega$) between the as-grown few-layer MoS_2 ($\Delta\omega \sim 26.1$ cm^{-1}) and the thinned MoS_2 ($\Delta\omega \sim 21.0$ cm^{-1}) confirms the few-layer MoS_2 has been trimmed down into monolayer. As shown in (d), a strong PL peak at ~1.87 eV is only observed on the film after the thinning process (which is the indication of the monolayer MoS_2 formation with direct bandgap), while no PL emission is detectable in the as-grown film. The comparable PL intensity detected from different regions of MoS_2 film indicates that the thinned film is in the same thickness/layer number across the full wafer.

4. Material characterization (UV-VIS, Raman, PL and XPS spectra) on monolayer Co-WS_2.

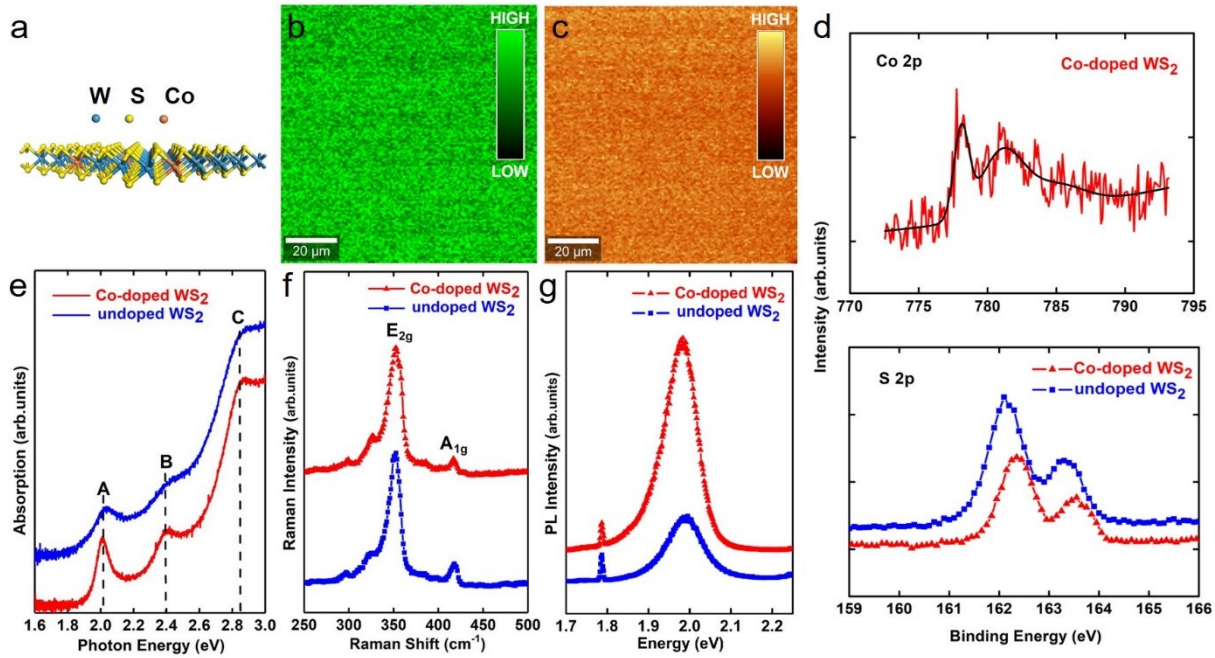

Figure S4. Self-limiting thinning method extend to the growth of monolayer Co-WS_2. (a) A schematic drawing showing the structure of Co-WS_2, in which the tungsten atoms are substituted by cobalt. Mapping images of (b) Raman E_{2g} intensity and (c) PL intensity captured on Co-WS_2 grown on the sapphire. (d) XPS Co 2p (top) and S 2p (bottom) spectra of Co-WS_2. Comparisons of the optical behaviors between the as-grown PSS-WS_2 and Co-WS_2 in terms of their (e) optical absorption, (f) Raman features and (g) PL signals.

While the synthesis of large-scale doped monolayer TMDC on industry-compatible substrates is still in its infancy, several theoretical ab initio studies have predicted that Co-doped TMDCs are good material for spin-electronic applications due to the tunability of electrical and photoelectric properties.[3-5] Interestingly, our facile strategy can be further extended to other complex doped TMDC, such as cobalt-doped WS_2 (Co-WS_2). Here, 0.2-nm cobalt is pre-deposited on the WO_3/sapphire and large-scale Co-WS_2 is grown by self-limited method under pulsed sulfur supply. To confirm the realization of Co doped in WS_2, comparative spectroscopic investigations are performed on as-grown PSS-WS_2 and Co-WS_2, respectively, as shown in **Figure S4**. XPS is an ideal tool for determining the composition of elements and their chemical states within a material. The recognizable Co signal preliminarily confirms the formation of Co-WS_2 (**Figure S4d**). The

obvious S 2p peak shift of ~0.17 eV towards higher binding energy is observed in Co-WS_2, indicating that the Fermi level is closed to the conduction band minimum under Co doping. Meanwhile, comparing with PSS-WS_2, the redshift of UV-light absorption peak and A1g Raman peak are also observed due to the increased electron and exciton recombination (**Figure S4e** and **S4f**). In addition, Co-doping effect is also convinced by the redshift of PL spectrum as shown in **Figure S4g**.[5] The homogeneity of the WS_2/SiO_2 coated Si is shown from the large-scale optical microscopic image (**Figure S4b** and **S4c**). In short, large-domain Co-WS_2 have been synthesized by self-limited thinning progress and widen the possibilities for the construction of TMDCs with adjustable band gap.

5. Comparison of AFM topographic images between PSS-WS_2 and CSS-WS_2.

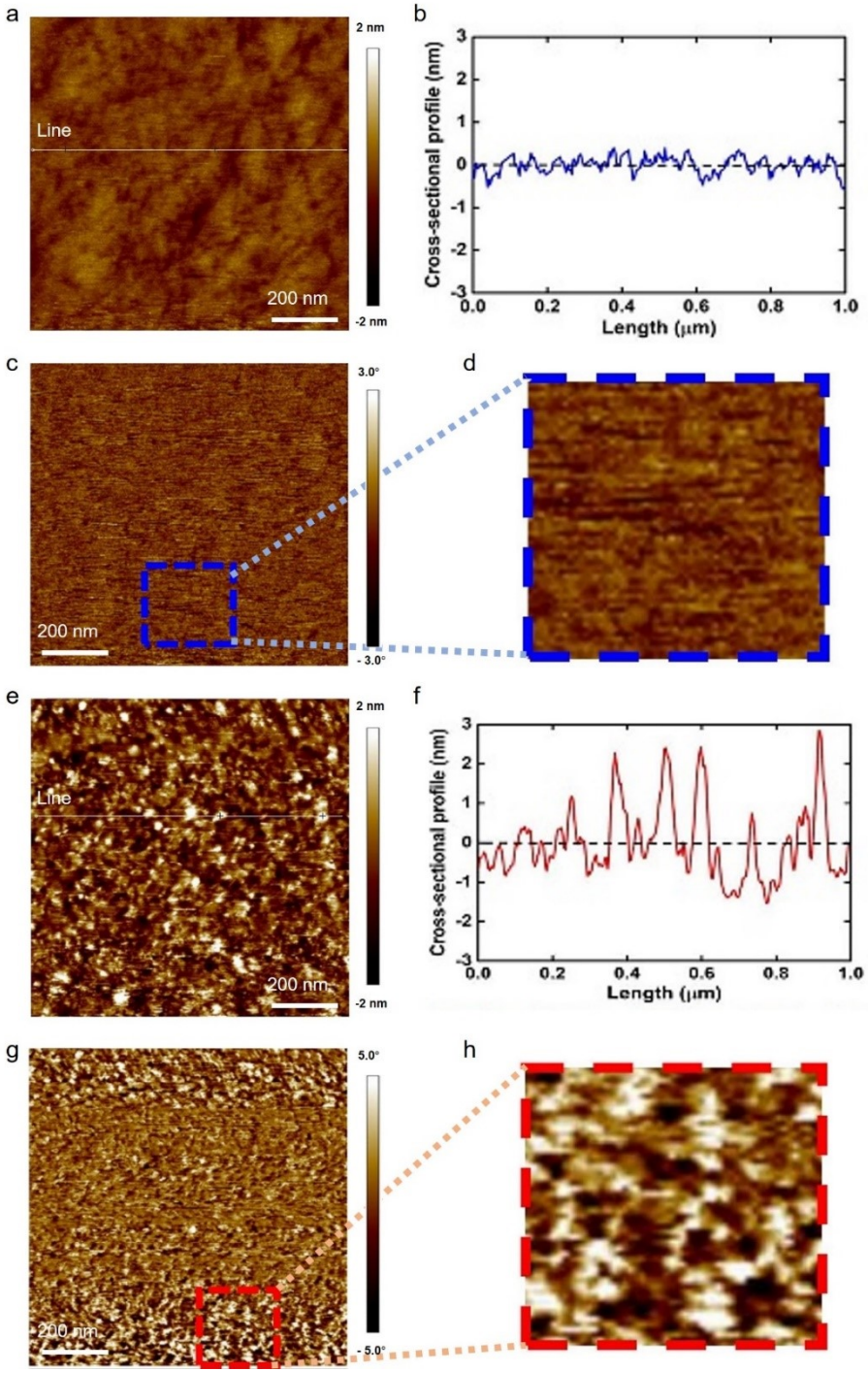

Figure S5. AFM images of (a-d) PSS-WS_2 and (e-h) CSS-WS_2. (a) and (e) The plane-view images, (b) and (f) the cross-sectional profiles extracted along the white line marked on plane-view images (a) and (e) respectively. (c, d, g, h) The phase images, while (d) and (h) are the enlarged images over the dashed box region in (c) and (g).

6. Comparison of PL, Raman and AFM images between PSS-WS_2 and WS_2 by PSS in the absence of H_2 gas.

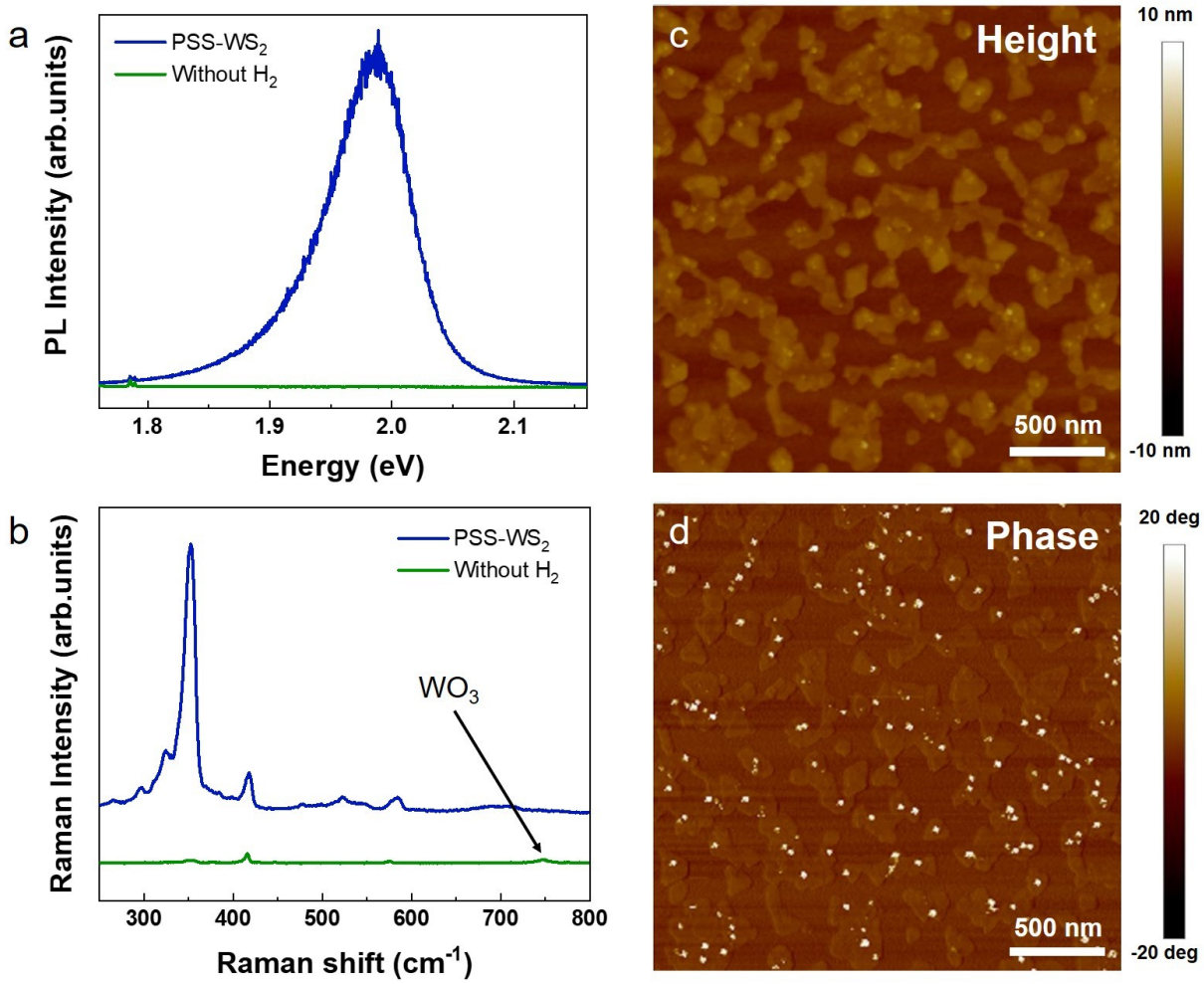

Figure S6. The characterization of WS_2 by PSS in the absence of H_2 gas. (a) PL spectra and (b) Raman spectra of PSS-WS_2 and WS_2 by PSS in the absence of H_2 gas. AFM (c) plane-view image and (d) phase image of WS_2 by PSS in the absence of H_2 gas.

7. Material characterization on PSS-WS_2 before and after high temperature annealing under constant flow of Ar + H_2 mixing gas without DES supply.

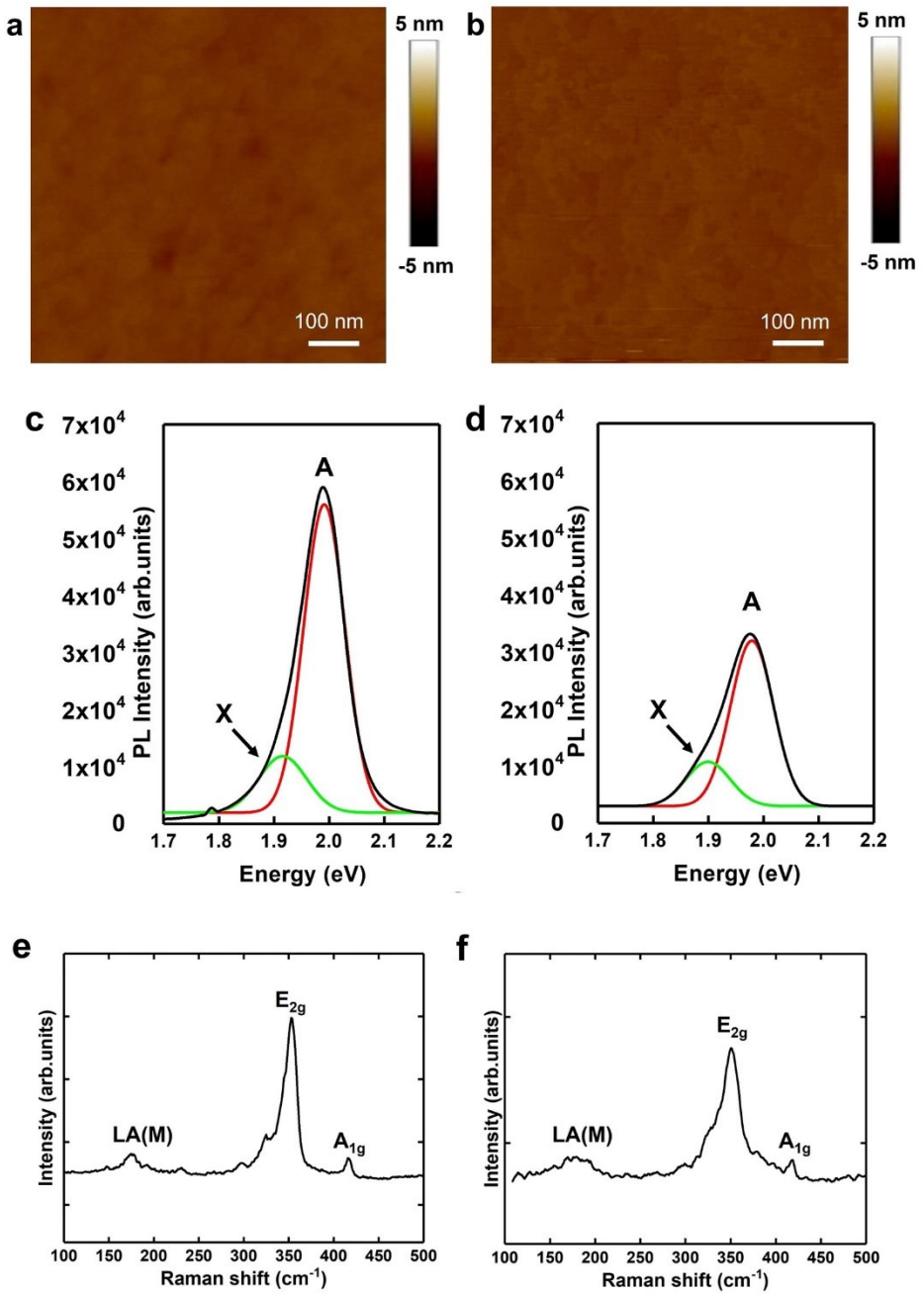

Figure S7. Material characterization on PSS-WS_2 on SAP (a, c and e) before and (b, d and f) after high temperature annealing at 1000 °C under constant flow of mixing gas (Ar/H_2) without DES supply for 20 minutes. (a-b) AFM plane-view topographic images, (c-d) PL spectra whereas the letters "A" and "X" refer to the emission due to A excitonic absorption and bound excitons X

trapped by the S vacancies respectively, (e-f) Raman spectra where peaks refer to E_{2g}, A_{1g} and LA(M) mode of WS_2 are indicated.

As shown in **Figure S7,** AFM images show that there is no significant morphological change on the WS_2 monolayer after high temperature annealing without DES supply. After the annealing, the surface roughness is only slightly increased from 0.214 nm to 0.253 nm as shown in **(a)** and **(b)** respectively.

The typical optical features of WS_2 monolayer, the predominant PL peak located at ~1.98 eV and the E_{2g} and A_{1g} Raman peaks with the separation of 62 cm^{-1} were unchanged, indicating the monolayer feature of the sample were unaffected after high temperature annealing. However, the annealing process has decreased the PL emission at ~1.98 eV (labelled as peak A in **(c)** and **(d)**) indicating the reduction in crystallinity of monolayer WS_2. The reduced crystallinity in the annealed WS_2 can be attributed to the increased S vacancies after annealing. It is known that the evolution of low-energy exciton PL peak X at ~ 1.89 eV and Raman LA(M) peak located at ~174.7 cm^{-1} happens with the increasing number of S vacancies in WS_2 films.[1-3] Thus an observation of the increased areas of both exciton PL peak X and Raman LA(M) peak as shown in **(d)** and **(f)** indicates that the number of S vacancies increase after annealing the monolayer WS_2. Indeed, the value of area ratio of A_X / A_A is increased from 0.212 to 0.277 where A_X and A_A are denoted as the area of PL peak X and PL peak A respectively as shown in **(c)** and **(d)**. Similarly, the value of area ratio of $A_{LA(M)}$ / A_{E2g} is also increased from 0.117 to 0.188 where $A_{LA(M)}$ and A_{E2g} are denoted as the area of Raman LA(M) peak and E_{2g} peak respectively as indicated in **(e)** and **(f)**.

8. Material characterization on PSS-WS_2 on SiO_2/Si.

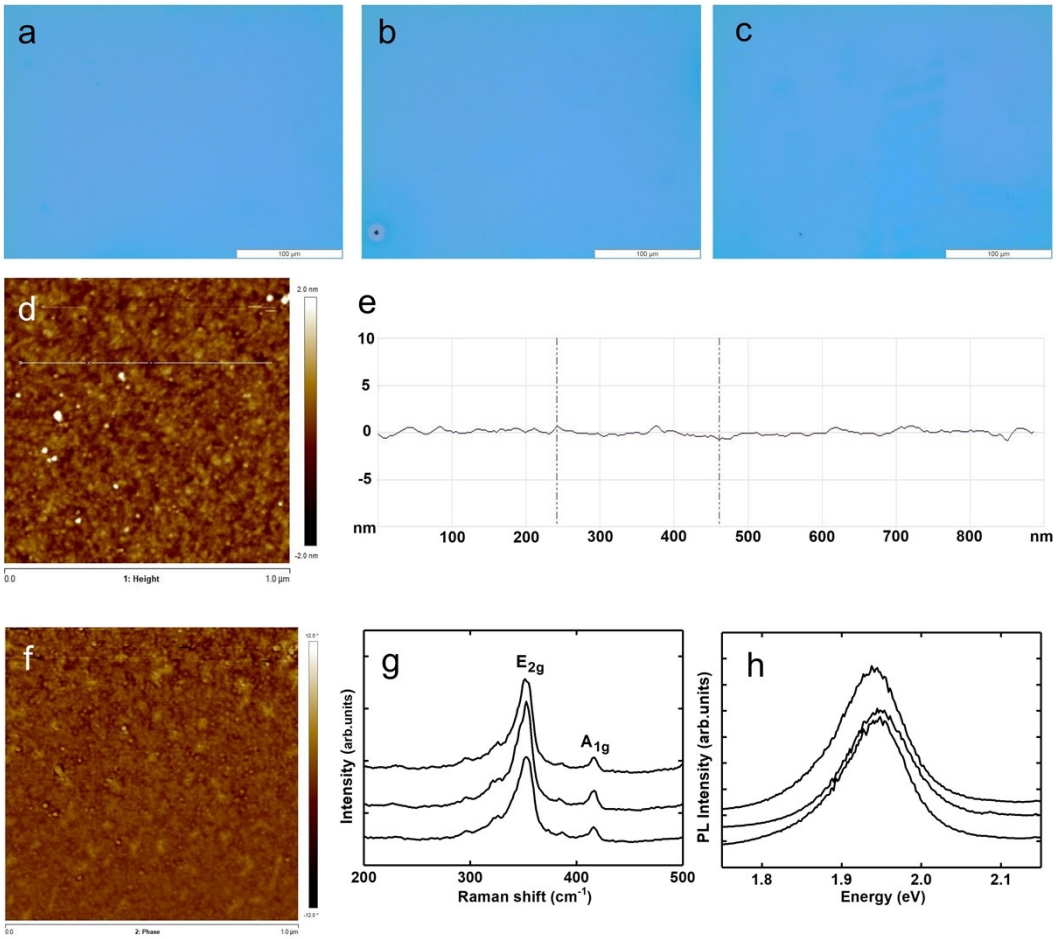

Figure S8. Material characterizations of PSS-WS_2 on SiO_2/Si. (a-c) Optical images captured from three different locations on PSS-WS_2 surface (scale bar 100 μm). AFM topographic images in (d) plane-view, (e) cross-sectional profile along the dashed line in plane-view AFM image and (f) phase imaging. (g) Raman and (h) photoluminescence spectra measured from three random locations on PSS-WS_2 surface.

9. **Raman spectra of MoS_2 on SiO_2/Si (a) before and (b) after the self-limited thinning process at a temperature of 950 °C.**

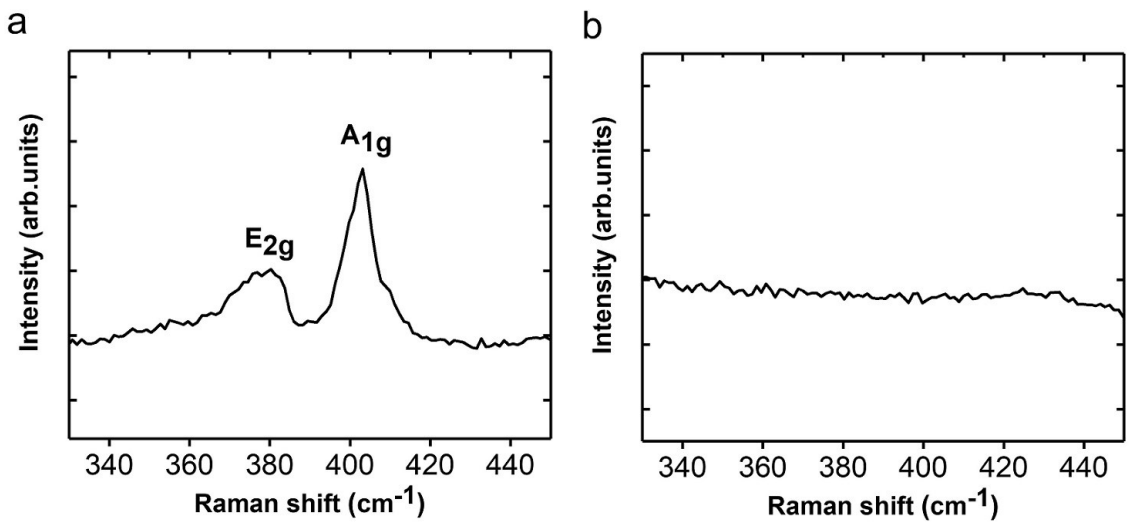

Figure S9. Raman spectra of MoS_2 on SiO_2/Si (a) before and (b) after the self-limited thinning process at a temperature of 950 °C. The as-grown MoS_2 film prepared by PVD sputtering process is in few-layer thick which have been reported in our previous works.[1,2] After the thinning process, no Raman peak is detectable from the sample which indicates that the formation of monolayer MoS_2 fails on SiO_2/Si due to the complete stripping-off of MoS_2. The instability of monolayer MoS_2 on SiO_2/Si is most likely due to the weaker binding energy of MoS_2–SiO_2 interface than that for MoS_2–sapphire interface.

10. Schematic drawing of bottom-gate-top-contact WS2 FET structure.

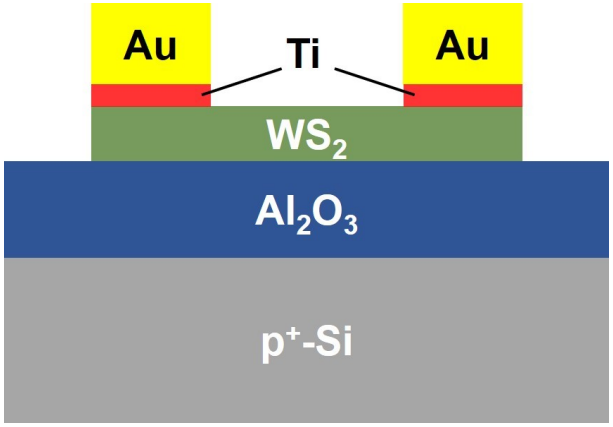

Figure S10. Schematic diagram showing the structure of bottom-gate-top-contact WS_2 FET.

11. Comparison of the electrical characteristics between PSS-WS2 FETs and CSS-WS2 FETs.

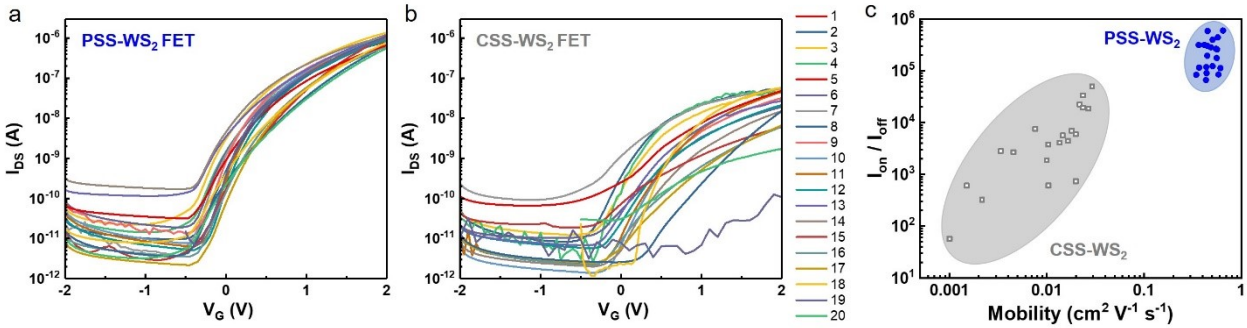

Figure S11. Electrical characteristics comparison between PSS-WS_2 and CSS-WS_2. The representative transfer characteristic curves of the FETs based on (a) PSS-WS_2 and (b) CSS-WS_2. (c) The statistics of field effect mobility and I_{on}/I_{off} ratio of FETs based on 20 groups of devices.

Table S1. The mobility is calculated by the FET model and following parameters.

$$I_{DS} = \frac{W}{2L}\mu C_{ox}(V_G - V_{th})^2$$

where μ, C_{ox}, W, L, and V_G, V_{th} are the field effect mobility, gate capacitance, channel width, channel length, gate voltage and threshold voltage, respectively.

Parameters	**Units**	**Numbers**
C_i	F cm^{-2}	2.29E-7
W	μm	200
L	μm	25

REFERENCES

(1) W. Yang, *et al.* Interlayer interactions in 2D WS_2/MoS_2 heterostructures monolithically grown by *in situ* physical vapor deposition, *Nanoscale*, 2018, **10**, 22927-22936.

(2) J. Tao, *et al.* Growth of wafer-scale MoS_2 monolayer by magnetron sputtering. *Nanoscale*. 2015, **7**, 2497-2503.

(3) J. Gao, *et al.* Transition-Metal Substitution Doping in Synthetic Atomically Thin Semiconductors. *Adv. Mater.* 2016, **28**, 9735-9743.

(4) H. Li, *et al.* Reducing Contact Resistance and Boosting Device Performance of Monolayer MoS_2 by In-Situ Fe Doping. *Adv. Mater.* 2022, **34**, 2200885.

(5) K. Dolui, *et al.* Possible doping strategies for MoS_2 monolayers: An ab initio study. *Phys. Rev. B* 2013, **88**, 075420.